Development of the fundamental power coupler for 324 MHz superconducting cavities

Mengxu Fan,[1,2,3,*] Huachang Liu,[1,2,3] Xiaolei Wu,[1,2,3] Yao Yang,[1,2,3] Shunming Liu,[1,2] Ahong Li,[1,2,3] Yun Wang,[1,2,3] Bo Li,[1,2] Peihua Qu,[1,2] Qiang Chen,[1,2] and Sheng Wang[1,2,3]

[1]*Spallation Neutron Source Science Center, Dongguan 523803, China*
[2]*Institute of High Energy Physics, Chinese Academy of Sciences (CAS), Beijing 100049, China*
[3]*University of Chinese Academy of Sciences, Beijing, 100049, China*

(Received 20 June 2023; accepted 21 August 2023; published 6 September 2023)

The China Spallation Neutron Source upgrade project (CSNS-II) has completed the preliminary design report and is expected to start in the fall of 2023. It plans to add two types of superconducting cavities: the 324-MHz double spoke superconducting cavity and the 648-MHz elliptical superconducting cavity in the linac section of the accelerator to upgrade the beam power from 100 to 500 kW, requiring more than 40 new fundamental power couplers (FPCs). These couplers will operate at pulse mode with a peak power ranging from 100 to 380 kW. To master the entire R&D process of the FPC for superconducting cavities, meanwhile, provide the horizontal test condition for various superconducting cavities research, a pair of 324-MHz power couplers for the double spoke superconducting cavity are developed. This coupler is a coaxial structure with a disk-warm ceramic window, and its characteristic impedance is 50 Ω. Multiphysics design is performed to ensure that the coupler meets the actual requirements. Structures of the coupler are optimized to realize a clean assembly with the cavity in Class 10 clean room and avoid window failure due to the bombardment of electrons generated by possible cavity field emission. We have successfully fabricated two FPCs and high power conditioned them on the test bench at room temperature. The test results show that FPCs can transmit a peak radio frequency (rf) power of 2 MW with a duty factor of 1.625% in traveling wave mode and an rf power of 500 kW with a duty factor of 3% in standing wave mode with arbitrary reflection wave phase. It meets the requirement of spoke cavities for CSNS-II—200 kW maximum power with a duty factor of 3%. Multipacting (MP) zones found during the high-power conditioning agree reasonably well with those predicted by simulations.

DOI: 10.1103/PhysRevAccelBeams.26.090401

I. INTRODUCTION

The China Spallation Neutron Source (CSNS) project reached the design parameter with a beam power of 100 kW in 2020 and has been stably operating for more than 3 years [1]. To increase the beam power from 100 to 500 kW in the CSNS upgrade project (CSNS-II), the linear accelerator section of CSNS consists of a 50-kW ion source, a 3-MeV radio frequency quadrupole (RFQ), and an 80-MeV drift tube linac (DTL) will be expanded. Two types of superconducting cavities: the 324-MHz double spoke cavity and the 648-MHz elliptical cavity will be used after the DTL cavity to upgrade the beam energy from 80 to 300 MeV [2,3]. Twenty 324-MHz double spoke cavities require a total power of 3.4 MW to accelerate the beam with an average beam current of 30 mA after 60% beam cutting (pulse width 600 μs, repetition rate 25 Hz) and achieve a beam energy gain of 85 MeV. A strong coupling with an external quality factor (Q_e) of 3.5×10^5 between the power source and the superconducting cavity is needed. This is realized by mounting a fundamental power coupler (FPC) on each double spoke cavity. At the same time, a test platform for superconducting cavities is now under construction at the CSNS campus, which will provide the necessary conditions for the development of CSNS-II and the research of different types of superconducting cavities. A power coupler with high power capacity is also needed for the horizontal test of superconducting cavities. Many coupler schemes were considered, a 324-MHz coaxial-type coupler with a single TRISTAN window and fixed coupling was finally chosen [4–6].

As one of the most important components of the superconducting cavity system, power couplers undertake the task of power transfer and vacuum barrier between the power source and the superconducting cavity. Since superconducting cavities always work in a cryogenic

*fanmx@ihep.ac.cn

environment, power couplers also play a role in the thermal transition from normal temperature to cryogenic temperature. All these features make the FPC one of the most complex components in a superconducting radio frequency system. Many aspects should be considered during the development of the FPC and three aspects as follows are mainly focused. First, the performance of superconducting cavities is often limited by its internal cleanliness, this requires that the vacuum part of power couplers should be proceeded and assembled in Class 10 clean room. The high power conditioning process should also be performed to verify the FPC function and to avoid cavity contamination due to vacuum bursts before the FPC is assembled with the cavity [7]. Second, power couplers operating in this frequency band are generally installed on the cavity wall rather than the beam tube, the position of the ceramic window and the structure of the coupler should be fully optimized to avoid the bombardment of high energy electrons generated by the field emission (FE) inside the superconducting cavity [8]. Third, the coupler must have sufficient margin for the stable operation of the CSNS-II as a user facility. Considering these aspects, the development of FPC for superconducting cavities involves aspects like clean process control [9], rf coupling [10], multipacting (MP) suppression [11,12], cryogenic heat loads [13,14], geometry optimization [15], safe design margins and so on, which are quite challenging.

In this paper, we mainly focus on the development of the 324-MHz fundamental power coupler (FPC) for superconducting cavities. This coupler not only meets the requirement of long-term stable operation of CSNS-II but also satisfies the needs of superconducting cavities test near the frequency of 324 MHz. The design parameters of the FPC are summarized in Table I. The rf design, thermal analysis, and cooling design are described in Sec. II. In Sec. III, MP simulation in two regions was executed with materials processed in different environments to predict MP zones. Mechanical analysis under different conditions was carried out and two prototype FPCs were fabricated, as described in Sec. IV. After that, FPCs were assembled on a test bench, and the high power conditioning process was performed in both traveling and standing wave modes. The FPC is finally conditioned to a peak rf power of 2 MW with a duty factor of 1.625% in traveling wave mode and a power of 500 kW with a 3% duty factor in full standing wave mode. MP barriers that reasonably match well with predictions are encountered and cleaned by conditioning. These are discussed in Sec. V. In the end, some conclusions are outlined in Sec. VI.

TABLE I. Design parameters of the FPC.

Parameter	Value
Frequency	324 MHz
Maximum power per FPC	400 kW
Duty factor	3%
Q_e	3.5×10^5
Operation mode	Traveling and standing wave
FPC type	Coaxial, single window
Coaxial line impedance	50 Ω
Number of FPC per cavity	1
Ceramic window material and type	Alumina, disk with choke
Coupling type	Antenna

II. FUNDAMENTAL POWER COUPLER DESIGN

The design purpose of the FPC is to minimize the reflection at the operating frequency, avoid the FE effect from cavities, control the cryogenic heat loads, provide a maximum safety margin, and many other aspects [16]. A coupled analysis of multiphysics including electromagnetic, thermal, stress, cooling, etc. is needed. The electromagnetic design of the FPC is described first, and the optimization of the FPC's overall transmission, bandwidth, and arcing probability is mainly focused in this section. The thermal and stress analysis is then performed, followed by the cooling design for different parts. To minimize the heat loss from normal temperature (298.15 K) to cryogenic temperature (2 K), the outer conductor inside the cryostat with a double stainless steel wall and thin copper plating is cooled by helium gas. In addition, air-cooled and water-cooled paths are also designed to ensure the stable operation of the FPC. The layout of the FPC is shown in Fig. 1. The CST Microwave Studio [17] is used for electromagnetic design, and the ANSYS [18] is used for thermal, stress, and cooling analysis during the development of the coupler.

A. Electromagnetic design

1. Doorknob

The main part of the FPC is based on a 50-Ω coaxial line. The existing 324-MHz power source system is to be used for FPC's high power conditioning. Its transmission waveguide is WR2300, so a doorknob is designed for the

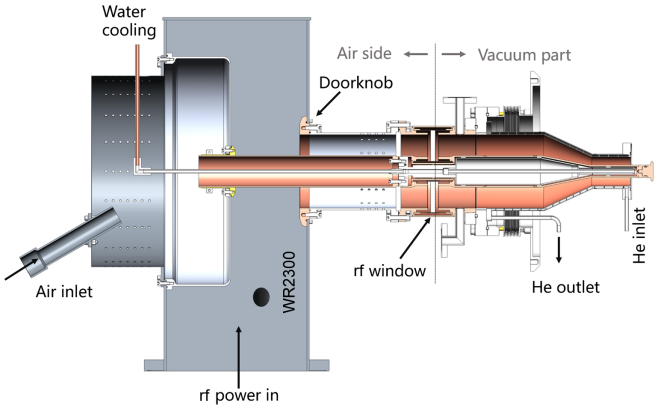

FIG. 1. Section view of the FPC assembly.

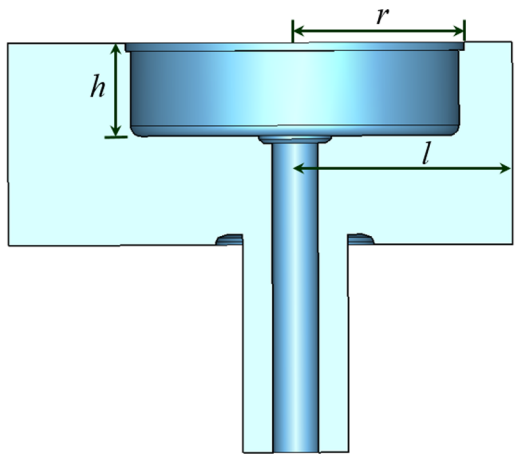

FIG. 2. Electromagnetic simulation model of the doorknob and optimization parameters.

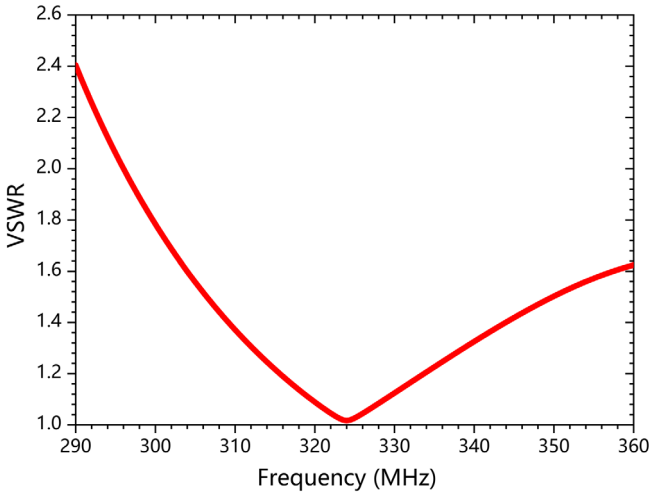

FIG. 3. Simulated VSWR of the doorknob.

transition from WR2300 to 6-1/8 in. coaxial line. To get a minimum reflection, we optimized the dimensions of the doorknob: the seat radius r, the seat height h, and the distance from the coaxial line to short wall l, as shown in Fig. 2. The optimized voltage standing wave ratio (VSWR) of the doorknob is shown in Fig. 3. The WR2300 waveguide and outer conductor of the coaxial line in the air side are made of 6061 aluminum alloy to lighten the weight of the FPC. The seat is plated by copper and the inner conductor of the coaxial line in the air side is made of pure copper to reduce the power loss and arcing probability.

2. rf window

The rf window is a key component of the FPC. The design of the rf window was derived from KEK-B FPC for superconducting cavities [4]. Due to the introduction of choke structure as impedance matching, brazing joints are in a position where the electric field is relatively weak, which greatly reduces the occurrence of sparking. Meanwhile, the electromagnetic field on the surface of the ceramic window with the choke structure is lower than that without the choke structure, which is helpful for the operation of the rf window [19]. The vacuum barrier of the rf window was a 10-mm thick disk-type ceramic window made of 97.6% purity Al_2O_3. To minimize the MP effect, the vacuum side of the ceramic window was plated with 10 nm TiN_xO_y. The choke node height hc and the distance between the ceramic and the choke node dc shown in Fig. 4 were optimized to obtain a reasonably low electric field at the brazing area and choke node. The variation of the magnitude electric field on the surface of the ceramic window along x direction before and after optimization under a peak forward power of 1 W is illustrated in Fig. 5. During the simulation, a dielectric constant of 9.4 was chosen as it had a limited effect on the rf performance [20]. The dimensions of hc and dc were optimized to 24 and 5.8 mm, respectively. Consequently, a peak electric field of 0.26 MV/m at the brazing joint between the ceramic window and the inner conductor and 0.76 MV/m at the choke node were obtained when 2-MW peak power was transmitted through the FPC. This was quite smaller than the breakdown field of 3 MV/m in the atmosphere.

3. Coaxial section and coupler transmission

The diameter of the coupling port on the cavity wall was initially chosen to be 60 mm, and a 100-mm long tapered structure was chosen to achieve the transition between

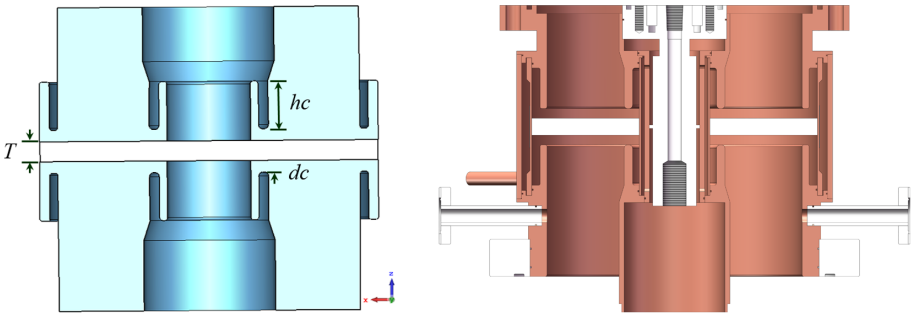

FIG. 4. Electromagnetic simulation model (left) and mechanical model (right) of the rf window.

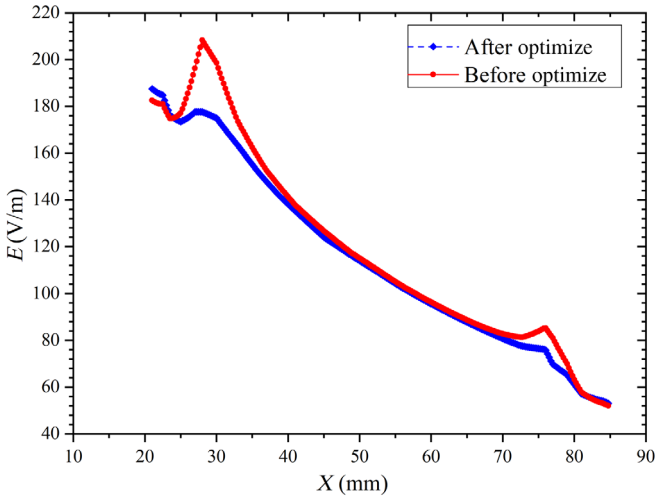

FIG. 5. The initial and optimized electric field distribution along the x direction with a peak forward power of 1 W passing through.

the 6-1/8 in. coaxial line and the 60-mm coaxial line. The tapered section was placed close to the coupling port and away from the ceramic window as it was prone to the MP phenomenon [21]. Since the coaxial line in the vacuum part of the FPC takes on the task of a thermal bridge from normal to cryogenic temperature, its length shall be as long as possible to minimize the static thermal load. However, the outer conductor length of the FPC shall be reasonably short to allow the preassembled coupler and superconducting cavity to be pushed into the cryostat. It requires the distance from the center of the ceramic window to the cavity wall shall be less than 510 mm. The choice of the window location is also relevant to the FE effect, it will be discussed in the following sections.

After the optimization of each component, the impedance match of the whole FPC containing the doorknob, the rf window, and the coaxial line was executed by slightly changing the parameters shown in Fig. 2. The electromagnetic simulation model and optimized return loss of the FPC are shown in Fig. 6. A bandwidth over 22 MHz was finally achieved when S11 was below −20 dB.

4. rf coupling and FE simulation

After the cavity beam dynamics analysis, its interaction with the coupler should be estimated. The double spoke cavity which will be used in CSNS-II is analyzed as an example in this section. Since the double spoke cavity operated in TEM mode, there was a strong electric field near the spoke bar area, and the direction of the electric field pointed to the coupling port as shown in Fig. 7. If there was an FE effect inside the cavity, the excited electrons might be accelerated to high energy and impacted on the ceramic window. Therefore, the antenna end of the FPC was enlarged, the coaxial line of the FPC was tapered and the diameter of the coupling port was chosen to be 60 mm as described above to avoid this harmful situation.

The insert depth (*Insert_l*) of the antenna should be fixed first before the FE simulation and its value was determined by Q_e. The optimal Q_e can be determined by the formula as follows [22]:

$$Q_e \approx \frac{V_c}{R/Q_0 \cdot I_0 \cos\varphi_s}, \tag{1}$$

where V_c is the voltage of the double spoke cavity of 5.07 MV, $I_0 = 30$ mA is the average beam current, $\varphi_s = -20°$ is the accelerating phase, R is the shunt impedance, Q_0 is the quality factor, and $R/Q = 410$. Considering the filling time of the cavity and the voltage oscillation of the cavity due to detuning, the coupling between the cavity with the accelerated beam and the FPC was often set to overcoupled rather than undercoupled, so the actual Q_e was

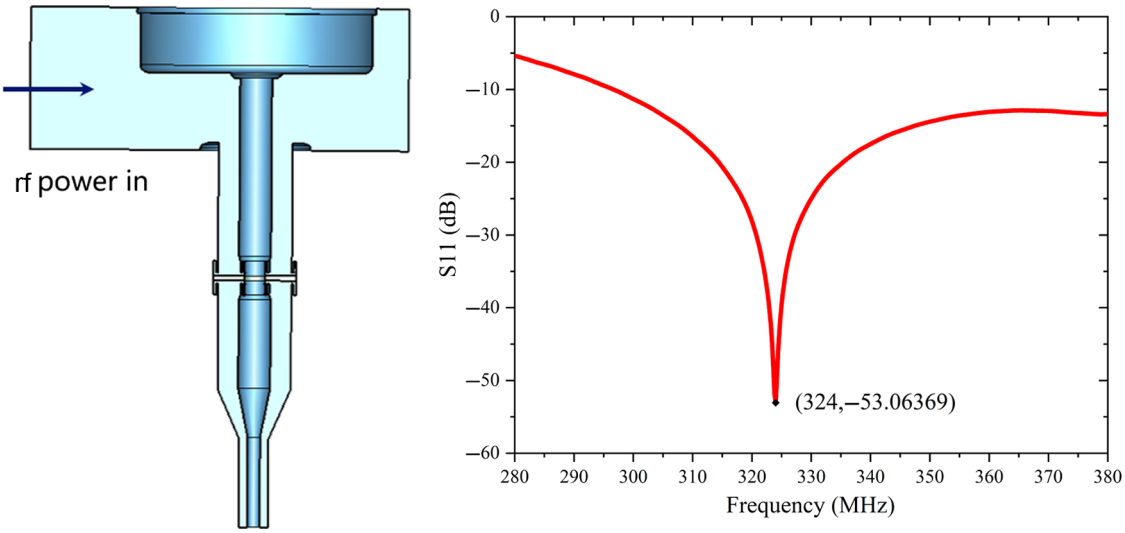

FIG. 6. Impedance match simulation model (left) and S11 parameter (right) of the FPC.

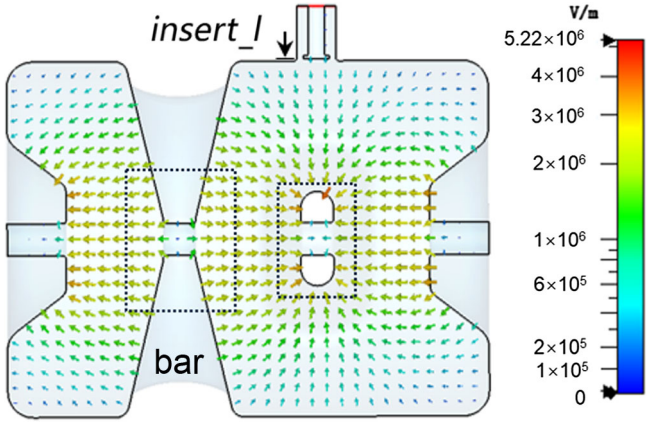

FIG. 7. The electric field distribution of the double spoke cavity with coupling port.

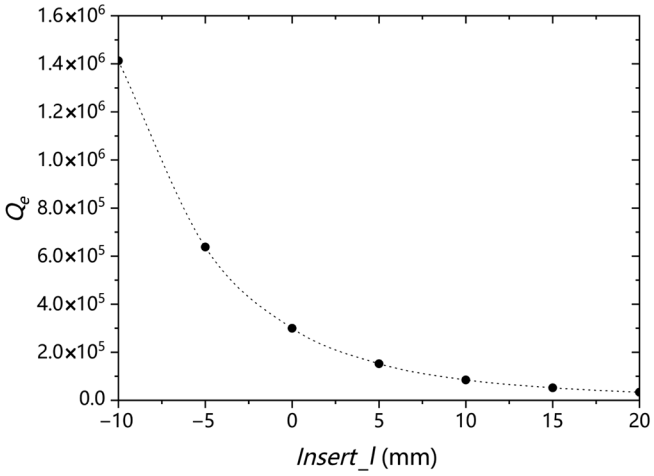

FIG. 8. The simulated Q_e vs *Insert_l*.

set a little lower than the optimal value and its value was chosen to be 3.5×10^5 [23]. The eigenmode solver in CST Microwave Studio is used for rf coupling simulation and the simulation model is shown in Fig. 7. The curve of simulated Q_e vs *Insert_l* is shown in Fig. 8. During the simulation, the reference position was the cavity wall, and the negative value of *Insert_l* indicated that the antenna end was away from the cavity and close to the coupling port, on the contrary, the antenna end was inside the cavity. Finally, Q_e reached the target value when the *Insert_l* was −1 mm.

The FE simulation was carried out in CST Particle Studio. The ceramic window position was initially placed at a nonmaximum electric field of the standing wave and could be slightly changed during the simulation. Generally speaking, electrons emitted by the surface of the spoke bar facing the coupling port are most likely to reach the ceramic window [8]. Initial electrons were therefore set on the surface of the spoke bar, trajectories of these electrons were tracked by sweeping the cavity voltage from 0.694 to 10.41 MV with a step of 0.694 MV and the relative rf phase from 30° to 360° with a step of 30°. Five plane monitors shown in Fig. 9(a) were placed along the z direction to mark the number of electrons accelerated to the FPC. Electron trajectories tracked at the operating cavity voltage of 5.07 MV are shown in Fig. 9(b). It indicated that only a small percentage of electrons flew into the FPC and impacted the inner conductor of FPC due to the tapered structure. The record electrons with different accelerating gradients (E_{acc}) are shown in Fig. 10. It indicated that electrons could only arrive at the "Pos_mt = 345" monitor when $E_{\mathrm{acc}} \leq 3$ MV/m and no electrons could reach the surface of the ceramic window ("Pos_mt" = 456.3 mm monitor) with any accelerating gradients. Considering the diameter of the cryostat for double spoke cavities was about 1.5 m and the preassembled FPC and spoke cavity should

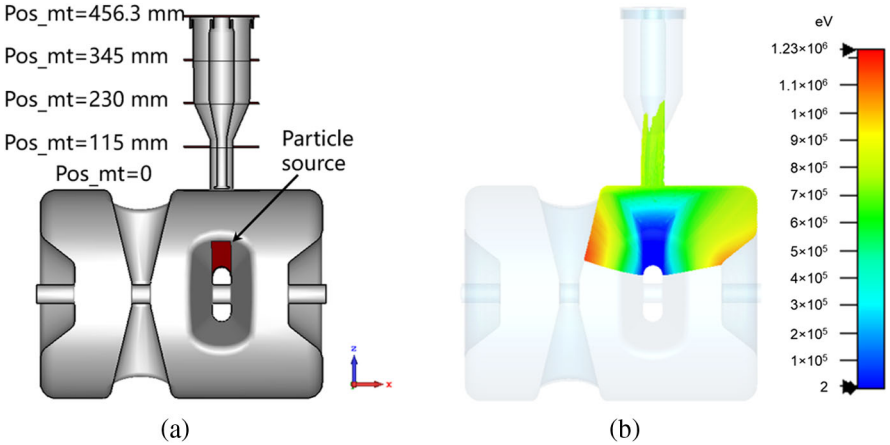

(a) (b)

FIG. 9. FE simulation setup and results: (a) simulation model, particle source, and plane monitors; (b) simulated electrons trajectories at 5.07-MV cavity voltage.

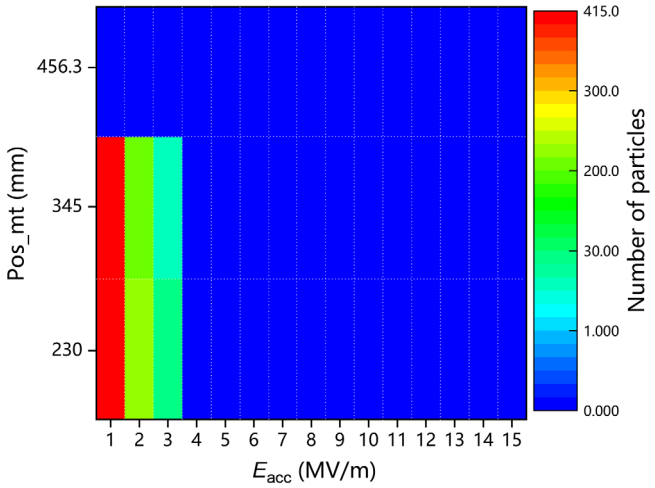

FIG. 10. Number of electrons hitting on different plane monitors.

be able pulled into the cryostat, as well as the ceramic window should be placed near the detuned-short position in the power transmission line to avoid the window failure due to overvoltage during a trip, the distance between the ceramic window center and the cavity wall was finally chosen to be 461.3 mm.

B. Thermal simulation and cooling design

The thermal analysis and cooling design of the FPC were executed after the electromagnetic design. To guarantee a maximum safety margin of the FPC, the forward power was chosen to be a 300-kW continuous wave (cw) in traveling wave mode during the analysis in this section. The rf loss was simulated with HFSS and imported to ANSYS for thermal-mechanical or fluid analysis. The initial simulation was performed with natural air convection to identify hot spots. The locations of temperature distribution from high to low were as follows: the inner conductor of the coaxial line in the vacuum part, the ceramic window, the outer conductor of the coaxial line in the vacuum part, the seat of the doorknob, and the outer conductor of the coaxial line in the air side. Different cooling methods were therefore used in these locations to control the temperature rise. Considering the operating temperature of different components for the FPC, the normal temperature part and the cryogenic part were analyzed separately by different methods. The gas cooling design of the FPC is summarized in Fig. 11.

There were two channels of forced air to cool the doorknob: one channel contained a pair of 34-mm diameter air inlets on the narrow side of the WR1500 waveguide, two air outlets on the short circuit of the WR1500 waveguide and the outer conductor of 6-1/8 in. coaxial line respectively, it was mainly used to cool rf surfaces of the doorknob; the other channel was on the shield of the doorknob and was to cool the non-rf surfaces of the

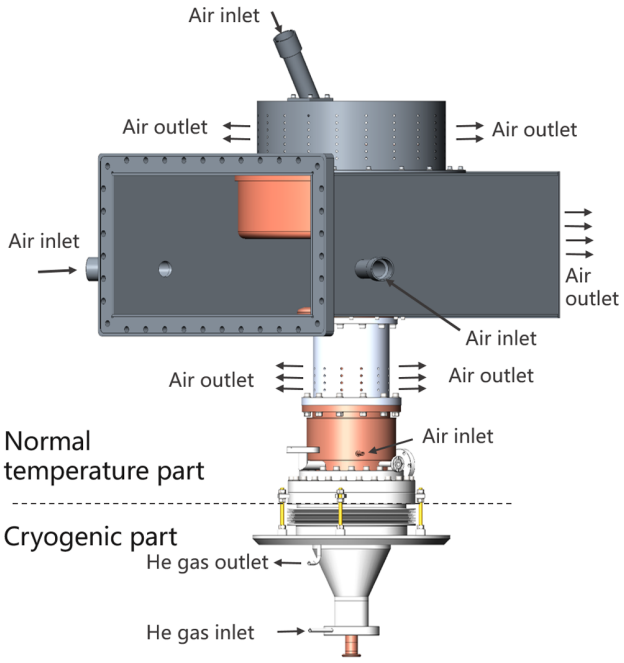

FIG. 11. The schematic diagram of the gas cooling design.

doorknob. To avoid the ceramic window surface contamination caused by long-term air cooling, a 10-mm thick disk-type Teflon was installed between the doorknob and the rf window. Considering that the temperature rise of the inner conductor of the rf window was greater than that of the outer conductor, the outer conductor of the rf window was cooled by forced air through an inlet port with a diameter of 6 mm, and the inner conductor of the rf window together with the inner conductor of the coaxial line in the vacuum part was cooled by water with a flow rate of 2 l/ min.

The doorknob's temperature distribution with two air cooling channels mentioned above when 300-kW cw power is transmitted through is shown in Fig. 12. The maximum temperature rise was in the inner conductor of

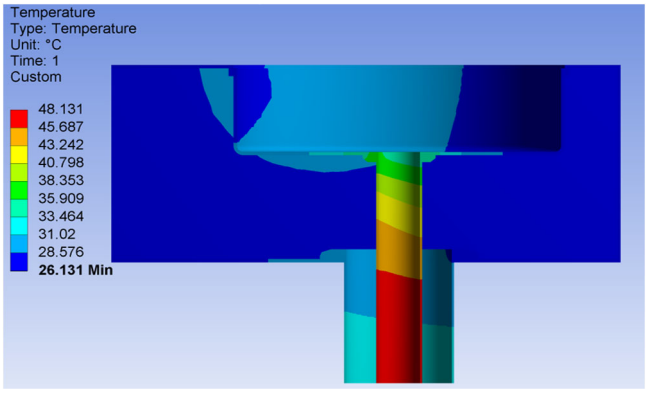

FIG. 12. Temperature distribution of the doorknob with 300-kW cw power passing through.

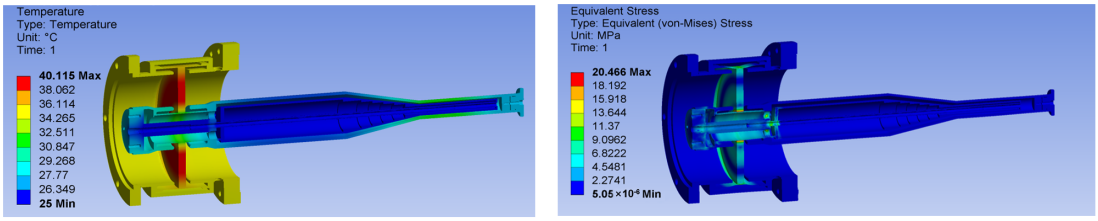

(a) (b)

FIG. 13. The temperature (a) and equivalent stress (b) distribution of the component consists of the rf window and inner conductor with 300 kW cw forward power passing through.

the coaxial line and it was about 0.77 °C for every 10-kW cw power increase.

The rf window and the inner conductor of the coaxial line in the vacuum part were analyzed together as they would be welded as one part. Multiphysics analysis containing the electromagnetic simulation, the thermal simulation, and the stress simulation was performed in ANSYS when 300-kW cw forward power was transmitted through in traveling mode. During the simulation, both the air and water cooling were added. The simulation results are shown in Fig. 13. The maximum temperature rise was in the middle of the ceramic window and it was about 15.115 °C. The maximum stress on the ceramic joint was about 20.466 MPa which was quite below the flexural strength of Al_2O_3 (296 MPa), and the location of it was at the brazing joint between the inner conductor and the ceramic window. Therefore, from the thermal and stress point of view, the design was feasible for the operation of CSNS-II.

The outer conductor of the coaxial line in the vacuum part undertakes a thermal bridge from normal to cryogenic temperature and is installed inside the cryostat. It means that both sides of the outer conductor are vacuum barriers and conventional cooling methods such as air and water cooling are no longer suitable. In addition, the length of the outer conductor is less than 350 mm, indicating that large heat loads need to be dealt with. The cooling design of the outer conductor is therefore quite challenging.

To control the cryogenic heat load and improve the cooling efficiency, a double-walled structure cooled by 5-K helium was applied as the outer conductor. The main material was chosen to be 316L stainless steel and a thin layer of 10-μm thick copper was plated on the surfaces exposed to rf power. Besides, a helical structure was brazed between double walls to guide the flow of helium. Copper plating was chosen because its high electric conductivity and large rf power dissipations on the stainless steel surface were unacceptable. The relationship between the average power dissipation (P_L) and the copper plating property can be described as follows [8]:

$$P_L \propto \frac{\frac{\sigma_{Cu}}{\alpha_{Cu}} + e^{-2d/\delta_{Cu}} \cdot \left(\frac{\sigma_s}{\alpha_s} - \frac{\sigma_{Cu}}{\alpha_{Cu}}\right)}{\left[\frac{\sigma_{Cu}}{\alpha_{Cu}} + e^{-d/\delta_{Cu}} \cdot \left(\frac{\sigma_s}{\alpha_s} - \frac{\sigma_{Cu}}{\alpha_{Cu}}\right)\right]^2}, \quad (2)$$

where σ is the electric conductivity, δ is the skin depth, α is the attenuation coefficient, d is the thickness of the copper plating, and the subscript "Cu" and "s" represents copper and stainless steel, respectively. The residual-resistivity ratio (RRR), as one of the parameters characterizing copper properties, is directly related to the electric conductivity of copper, which affects the power dissipation on the surface of the outer conductor and finally determines cryogenic heat loads [24]. So cryogenic heat loads were simulated with different RRR values. The simulation of cryogenic heat loads was achieved by multiple iterations between HFSS and Fluent. Considering the large aspect ratio of the simulation model, only the outer conductor is used for simulation, as shown in Fig. 14. The helium gas with a temperature of 5 K was fed into the cooling channels through an inlet port with a diameter of 6 mm. According to the simulation, a flow rate of 30 mg/s for the helium gas was required and the RRR for copper plating was about 30. Correspondingly, the FPC contributed about 0.47 W of heat loads at 2 K temperature to the cryogenic system when 300-kW cw forward power passed through. It should be

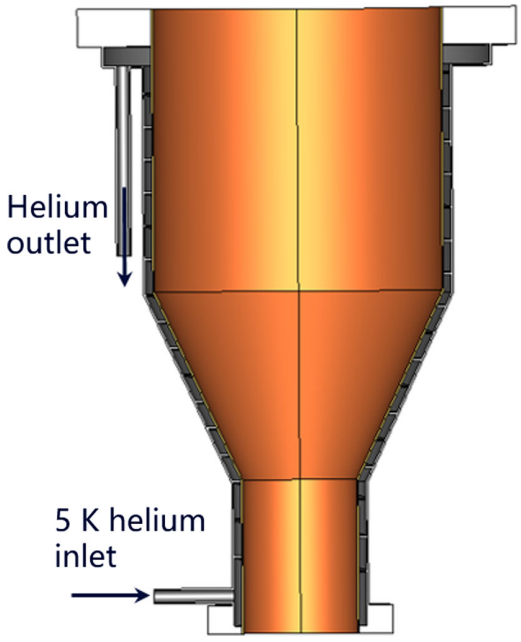

FIG. 14. The simulation model of the outer conductor.

noted that the heat loads calculated above contained static heat loads only due to the metal thermal conduction and dynamic heat loads due to power loading.

III. MULTIPACTING ANALYSIS

MP is a phenomenon in which free electrons are accelerated by the rf electric field built inside the device, impacting the surface of metallic or dielectric surfaces and eventually leading to an exponential growth of secondary electrons [25,26]. It may cause the degeneration of the FPC performance, and in the worst case, the ceramic window may fail [27]. On the one hand, for the rf superconducting accelerator system, the ceramic window failure is almost catastrophic. A series of tasks such as the disassembly of the superconducting cavity, processing of the cavity in the clean room, high power conditioning, etc. need to be redone. On the other hand, the reduction of rf accelerator operating efficiency due to the MP phenomenon in FPC is unacceptable as the CSNS-II project is a user facility [28]. MP analysis is therefore quite important in the design stage.

MP simulations were performed in CST Particle Studio and he PIC solver was used. Particle sources on two different areas shown in Fig. 15 were simulated: (a) the coaxial line region between the rf window and the coupling port; and (b) the rf window region with ceramic and choke structure. Received and argon-discharged copper materials were used in the simulation to distinguish the soft and hard MP barrier, where the received copper material was untreated and the peak secondary electron emission yield (SEY) of it was about 2.1 [29], while the argon-discharged copper material was equivalent to the copper material after high power conditioning and the peak SEY of it was relatively low. The difference between the soft and hard MP barriers is that the soft MP barrier can be eliminated through the high power conditioning process while the hard MP barrier cannot. Besides, the vacuum side of the ceramic window was usually coated by a thin titanium nitride (TiN) film to suppress MP. The SEY curve of TiN material depended on the quality of the coating process, so a relatively conservative SEY curve of TiN was used for simulation to greatly ensure the operation security of the ceramic window. SEY curves of three materials used in the simulation are summarized in Fig. 16. The external electromagnetic field used for MP simulation was simulated by the frequency domain solver in CST. During the electromagnetic simulation, the assembled coupler and superconducting cavity model were used and a waveguide port was set on the WR2300 waveguide, which meant the results simulated were working at standing wave mode, and the electromagnetic field distribution at this time was the same as that when the cavity worked at room temperature.

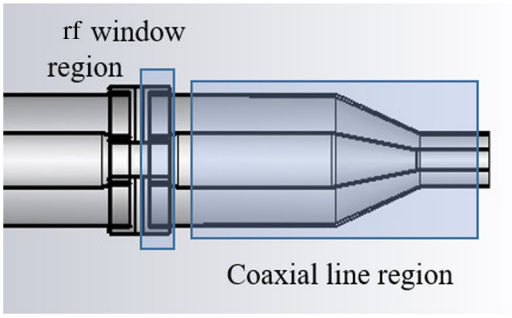

FIG. 15. MP simulation regions.

The input power was swept from 10 to 400 kW with a step of 10 kW during the MP simulation. The simulation results are shown in Fig. 17. We could draw the following conclusions from the simulation results: (i) In the coaxial line region, the 46-kW MP zone might be encountered on the outer conductor and 10–90 kW MP zones might be encountered on the inner conductor during the high power conditioning, and it might take a long rf conditioning time to eliminate MP between 15 and 40 kW due to the large SEY value. (ii) In the rf window region, 70–140 kW MP zones should be paid more attention during the high power conditioning, and we might not meet the MP phenomenon in other power ranges during the rf conditioning since the SEY curve changed gently and the peak value of it was relatively low. (iii) The simulated SEY values in this power coupler with argon-discharged copper material were all below 1, in other words, only soft barriers could be found in this design and they could be all eliminated by rf conditioning. It should be noted that MP was strongly dependent on the surface treatment, local structure, and electromagnetic field distributions, all of which made accurate prediction of MP quite difficult. Therefore, to ensure the safety of the rf conditioning process as much as possible, a dc bias would also be set between the inner and the outer conductor of the FPC to suppress MP barriers [31].

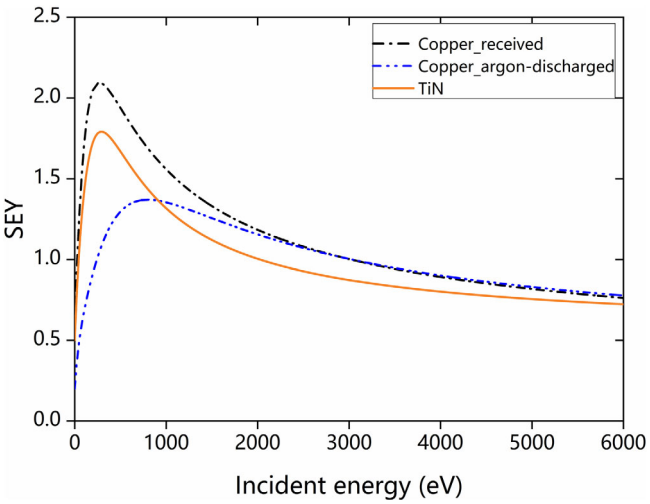

FIG. 16. The SEY curves of different materials used in the simulation [30].

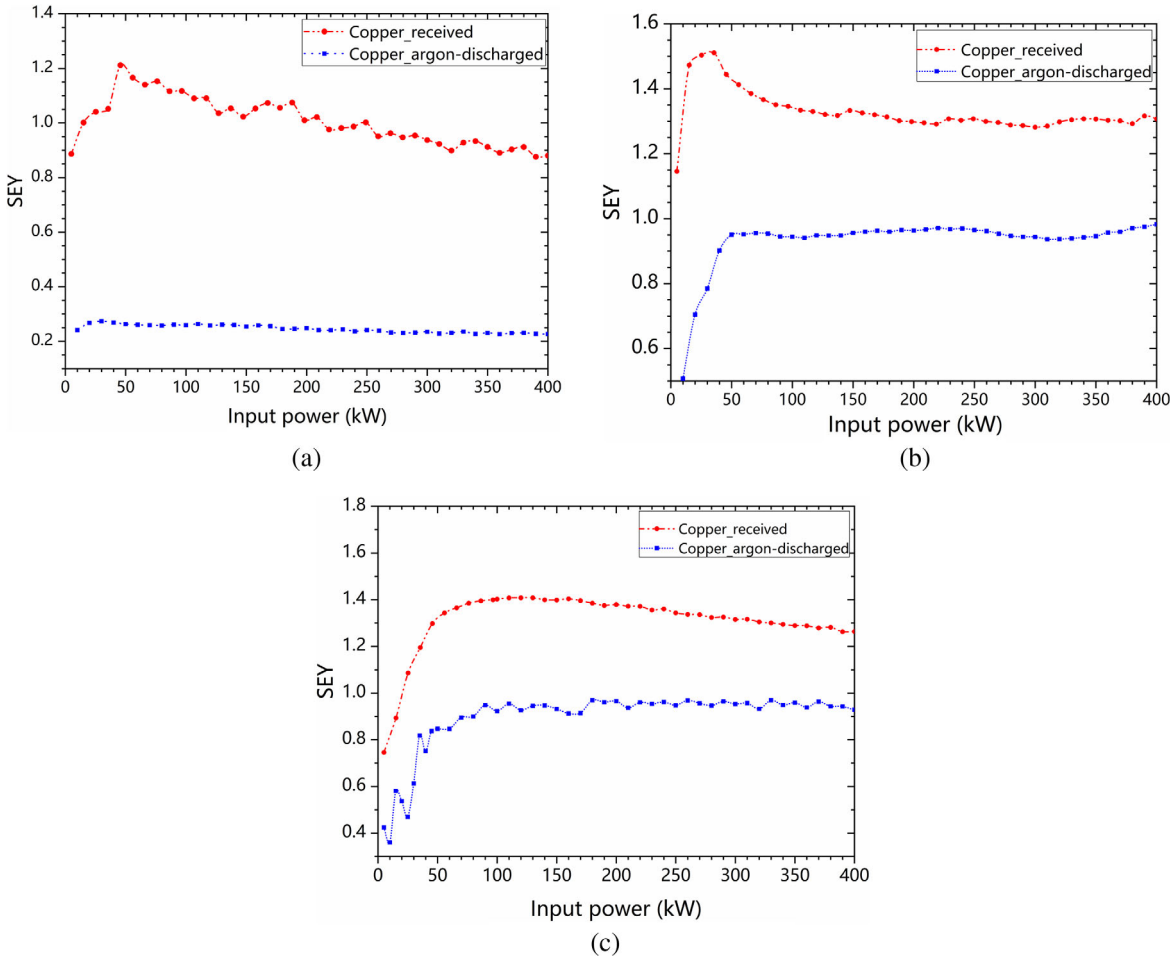

FIG. 17. MP simulation results. (a) MP simulation results in the coaxial line region with different processed materials when the initial particle source is set on the outer conductor; (b) MP simulation results in the coaxial line region when the particle source is set on the inner conductor; (c) MP simulation results in the rf window region with TiN and different processed copper materials.

IV. MECHANICAL DESIGN AND FABRICATION

The mechanical simulation model and boundary condition of the component consisting of the FPC rf window and the inner conductor are shown in Fig. 18. The inner conductor of the FPC was made of copper material and was cooled by water, the material of the water cooling structure was stainless steel, and the double-wall structure formed by the inner conductor and the water cooling structure provided a passage for water. The outer conductor of the rf window brazed together with the vacuum-sealed stainless steel flange was made of annealed oxygen-free copper and was cooled by forced air. To increase rigidity, the inner conductor near the ceramic window was reinforced with a cylindrical ring that was brazed to the inner conductor and had eight vertical rectangular holes.

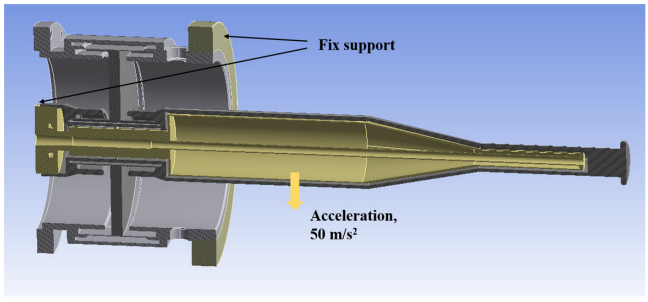

FIG. 18. Mechanical simulation model and boundary condition.

During the simulation, the rf window assembly flange and the end of the water cooling structure were fixed [32]. The first modal frequency of the rf window was 126.21 Hz and its corresponding degenerate mode frequency was 126.28 Hz, which was away from the integer multiples of the running repetition rate of 25 Hz. The second modal frequency was 548.84 Hz and its degenerate mode frequency was 548.94 Hz. The degenerate modes of these two modes are shown in Fig. 19 and they all met the design criteria. Due to the lateral assembly of the rf window, a 5 times gravity acceleration perpendicular to the inner conductor was applied to the whole rf window to analyze whether it met the safety requirements during

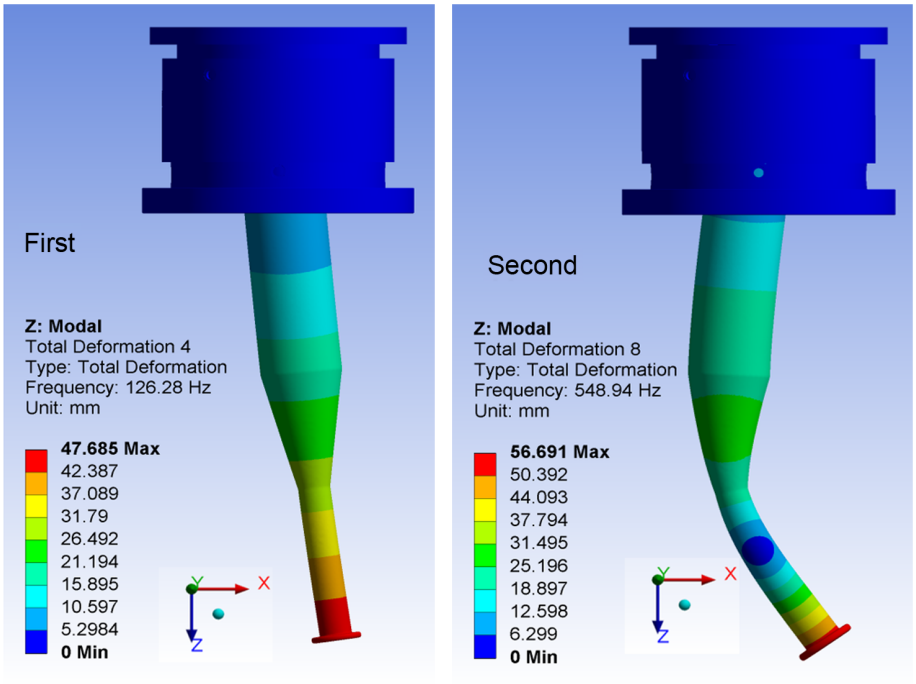

FIG. 19. Modal analysis results of the rf window.

transportation. According to the simulation result, the maximum stress of the annealed copper material component, the stainless steel material component, and the Al_2O_3 material component was 14.5, 28.1, and 16.7 MPa, respectively, and they were all smaller than their yield strength, as summarized in Table II. The maximum deformation occurred at the tip of the inner conductor and its value was only 0.1433 mm. Therefore, we could conclude that the mechanical structure of the FPC rf window assembly would meet the requirements of both shipment and accrual operation.

Two prototype FPCs were manufactured by Beijing HE-Racing Technology Co., Ltd. Various materials such as 6061 aluminum alloy, 316L stainless steel, oxygen-free high conductivity copper (OFHC), alumina ceramic, and various soldering procedures such as brazing, electron beam welding, tungsten inert gas (TIG) welding were used to guarantee the performance and lightness of the FPC. The WR2300 waveguide of the doorknob was welded together with 6061 aluminum alloy plates, and it was assembled with the outer conductor of the coaxial line in the air side and the seat plated by copper. As for the rf window, the ceramic window was brazed with two thin-walled cylindrical rings first to avoid the failure of the ceramic, then cylindrical rings were brazed to other components with different functions such as cooling, vacuum seal, reinforcement, and so on. The rf window after brazing is shown in Fig. 4. A 10-nm thin TiN layer was thereafter coated on the vacuum side of the ceramic window to suppress MP. The inner conductor of the FPC in the vacuum side was finally welded together with the rf window by the electron beam. The outer conductor of the coaxial line in the vacuum side was processed by the five-axis machine and welded by TIG welding. A 10- to 15-μm thick copper layer with a RRR value of 30 was plated to the inner surface of the double-walled outer conductor after that. To ensure the quality of copper plating, various samples were plated and tested to obtain the thickness and RRR values consistent with design requirements. The copper layer should be finally able to survive after high-temperature annealing and multiple thermal cycles from liquid nitrogen to air temperature.

TABLE II. Simulation results with 5 times gravity acceleration on the inner conductor [16].

Material components	Maximum stress (MPa)	Yield strength (MPa)
Annealed copper	14.5	33.1
Stainless steel	28.1	221.3
Al_2O_3	16.7	59

FPCs were finished in 7 months and key components were successfully brazed in just one attempt. Components, assemblies, and final couplers are shown in Fig. 20. After the fabrication, a series of tests were conducted. The test result showed that the leakage rate of the assembled coupler was better than 10^{-10} mbar · l/s, the ultimate vacuum after 72 h of baking was 2.3×10^7 Pa and all water cooling channels could withstand 6 bar water or air pressure for more than 3 h, which met the requirement for operation. We encountered a problem of coaxiality deviation between the inner and outer conductor of the FPC after assembly, which

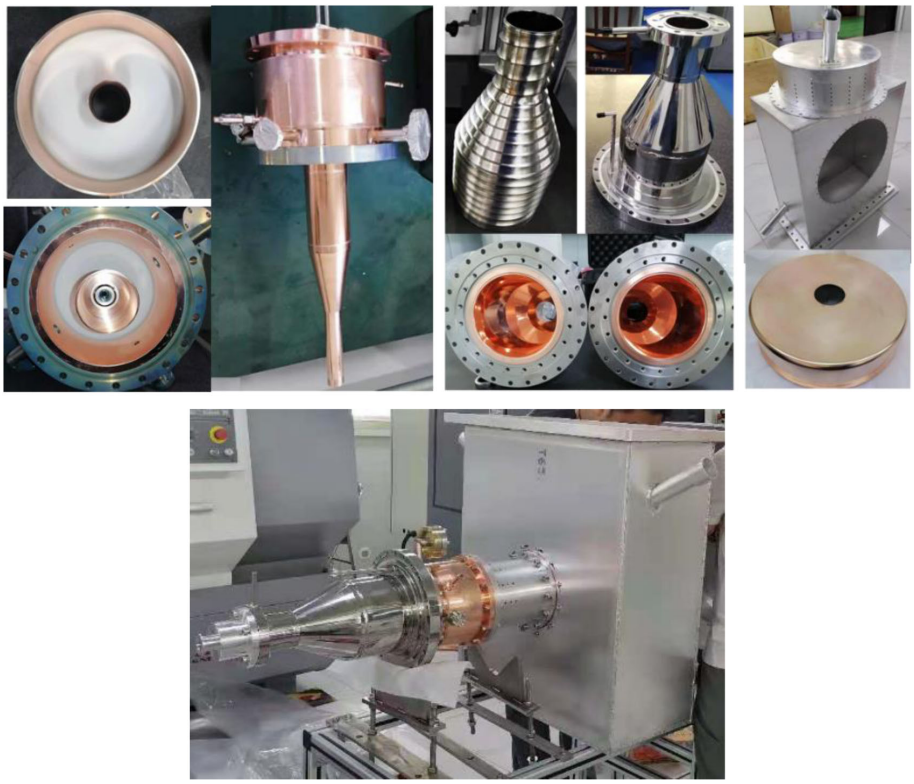

FIG. 20. FPCs' components and assemblies during the fabrication.

might lead to poor transmission. Improvement of the tooling for welding and assembly was considered for future FPCs.

V. PERFORMANCE VERIFICATION

Due to the high cleanliness requirements of the superconducting cavity, FPCs shall be high power conditioned to verify their functionality before they are assembled with the cavities. During this process, residual gas is removed, surface contamination is burned and MP barriers are all cleaned by conditioning, they are all helpful to maintain the cleanliness and improve the performance of the whole system consisting of couplers and superconducting cavities. In this section, we described the assembly, high power conditioning, and validation of the FPC in detail.

A. Assembly of the test bench

The test cavity, a compact quarter-wavelength matcher, was developed to achieve a good rf transmission between the up and down FPC, as shown in Fig. 21. Meanwhile, it also provided a vacuum port connected to the ion pump for an ultrahigh vacuum. The main body of the test cavity (cylindrical shape with two ports) was made of 316L stainless steel and was copper-plated on the surface exposed to the rf power, it was brazed together with a T-shaped structure (lid of the cavity) made of OFHC and cooled by water. Coupler installation ports on the test cavity were double-walled and water-cooled to control the temperature rise. The test cavity could finally transmit a cw power up to 500 kW.

A cleaning procedure was performed for both the FPC and the test cavity after fabrication [33]. All components in the vacuum part (the rf window, the double-walled outer conductor, the bellow, and the test cavity) were first ultrasonically cleaned with detergent-added ultrapure water. They were then rinsed with deionized water in a Class 10 000 clean room. After that, they were dried with high-purity nitrogen and placed for more than 24 h in Class 10 clean room. The doorknob and other components in the air side were cleaned with alcohol to remove the dust and grease after the fabrication. When everything was ready, the assembly process was followed. All components were finally assembled on a movable aluminum stand, as shown in Fig. 21. Components in the vacuum part and the 400 l/s ion pump were assembled in Class 10 clean room to avoid contamination, while other components were mounted in the regular environment. The transmission of the system shown in Fig. 22 was measured by connecting two WR 2300 to N waveguides, and the reflection coefficient was about −36 dB at 324 MHz, which was consistent with the simulation results.

The test bench was finally pulled to the target position, and it was assembled with the WR2300 waveguides connecting to the 2.5-MW klystron and the load or short plate, as shown in Fig. 23. The klystron used for high power

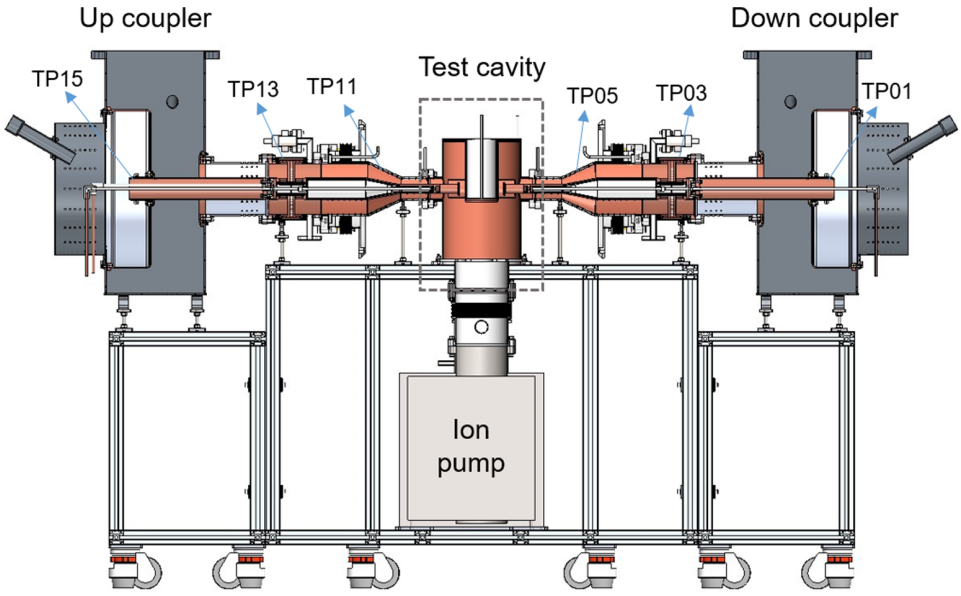

FIG. 21. The assembly test bench with two couplers. "TPxx" means the temperature probe.

conditioning was the same as that used in the CSNS DTL, it could provide a peak rf power of 2.5 MW with a duty factor of 1.625% and a power of 500 kW with a 3% duty factor. The test bench was therefore high power conditioned in both traveling and standing mode. Besides, various monitors were deployed on the test bench. Each coupler was equipped with a vacuum gauge, an MP monitor, and an arc detector to obtain the status of the FPC and avoid the failure of the ceramic window. We attached 15 temperature probes on the surface of FPCs and the test cavity to monitor the temperature rise, while 6 of them shown in Fig. 21 were mainly focused on. TP15 and TP01 represented the temperature of the inner conductor in the air side, an abnormal temperature of them might cause the insulating material to be burned; TP13 and TP03 were the temperatures of the rf window outer conductor, they could reflect the operating temperature of the ceramic window; TP11 and TP05 were the temperatures of the double-walled outer conductor, they could show whether there was MP phenomenon on the copper-plated structure. We also used four flow switches with temperature probes at the outlet to monitor the water flow rate and the temperature of the water after cooling. All these signals were aggregated into the control and interlock system to ensure the safe operation of the FPC during high power conditioning.

B. High power conditioning

The high power conditioning process started from a narrow pulse width of 100 s and gradually expanded to a pulse width of 1.2 ms and the repetition rate during

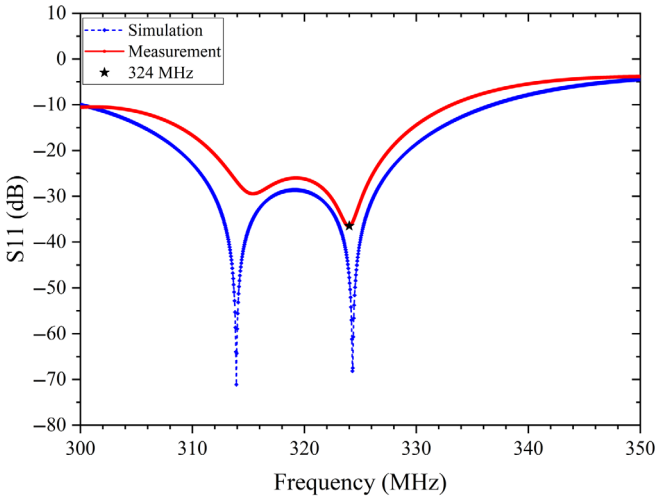

FIG. 22. Simulation and measurement results of the test bench.

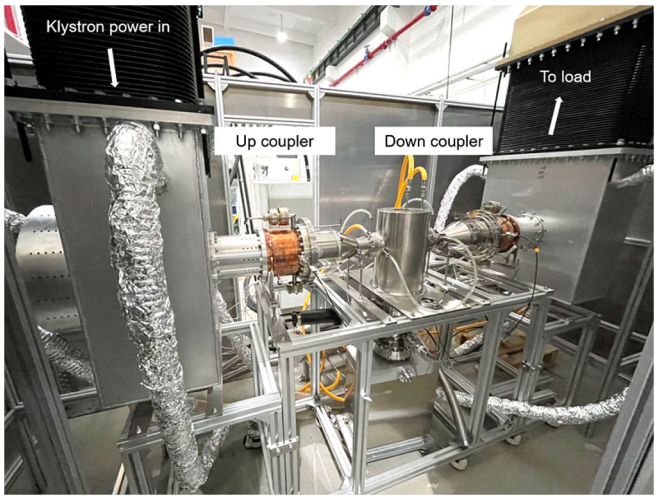

FIG. 23. The test bench setup for high power conditioning.

conditioning was kept to 25 Hz. FPCs were conditioned in both traveling mode with a peak power of 2 MW and standing wave mode with a peak power of 500 kW. Various activities such as vacuum bursts, arc discharging, local heating, and so on were observed. The rf interlock system was therefore always on during the conditioning to avoid damage to the coupler from these activities.

The software was developed for the convenience of high power conditioning [34,35]. It could automatically increase, decrease, and maintain the rf power according to vacuum levels. We defined four vacuum levels: V_A, V_B, V_C, and V_D, the relationship among these levels were V_D > V_C > V_B > V_A. The predefined algorithm in the software was as follows: the rf power was increased by a predefined step when the vacuum value was better than V_A (10^{-5} Pa); when the vacuum value was between V_B (5×10^{-5} Pa) and V_C (8×10^{-5} Pa), the rf power was decreased at a preset rate; if the vacuum was between V_C and V_D (10^{-4} Pa), the rf power was decreased rapidly to avoid the continued deterioration of the vacuum; the rf power was kept constant if the vacuum value was between V_A and V_B; if the vacuum was worse than V_D, the rf power was set to zero and it would be increased again only until the vacuum value was better than V_A. The software also provides a manual mode, which is quite useful for complex situations; and the automated conditioning process could be human intervened at any time.

The ambient temperature and the inlet water temperature were both 25 °C during the high power conditioning. Four water cooling channels were used for the test bench, two of them were used to cool the inner conductor of the rf window for up and down couplers, and the other two were used to cool the test cavity. A blower with a maximum flow rate of 27 m^3/min was chosen for the forced air cooling and the inlet temperature of the forced air was about 26.4 °C for the port with a diameter of 44 mm and 25.4 °C for the port with a diameter of 8 mm. There were five air cooling channels for each coupler. Taking air cooling channels for the up coupler as an example, one channel was used to cool the double-walled outer conductor, the other channels were consistent with that shown in Fig. 11. The acquired vacuum of the FPC was about 1.3×10^{-6} Pa before high power conditioning. Interlock signals such as vacuum, air and water cooling, temperature, arc, high voltage, and so on were all checked before the rf power was on.

rf power with a relatively low duty factor of 0.25% operating at traveling wave mode was first used for high power tests because of the strong vacuum burst of the test bench in the early stage, and the function of the whole system containing hardware and software needed to be verified. It took about 80 h (including problem-solving time) to reach the peak power of 2 MW, electromagnetic compatibility problems, and bugs in software were solved in this stage. The duty factor was then expanded to 1.625% and the system was quickly high power conditioned to the 2-MW peak power in traveling wave mode, the time consumption of this stage is about 15 h. The measured temperature rise of the rf window outer conductor and the air-side inner conductor was about 0.38 and 0.5 °C, respectively, for every equivalent 10-kW cw power. It was a little larger than the design because the used fan speed of the blower was only half of the design value. After that, the dummy load was replaced with the movable waveguide short circuit. The system was high power conditioned to 500-kW peak power with a duty factor of 1.625% in standing wave mode. To ensure the FPC was

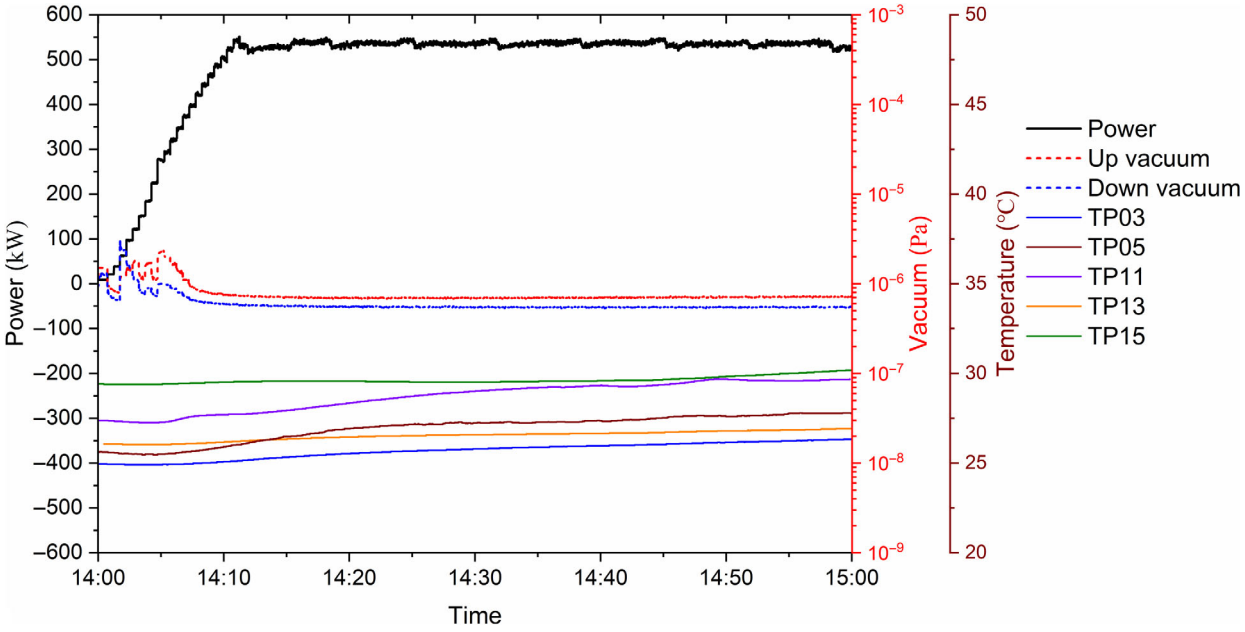

FIG. 24. The performance of the FPC operating in standing wave mode after high power conditioning. No dc bias is applied.

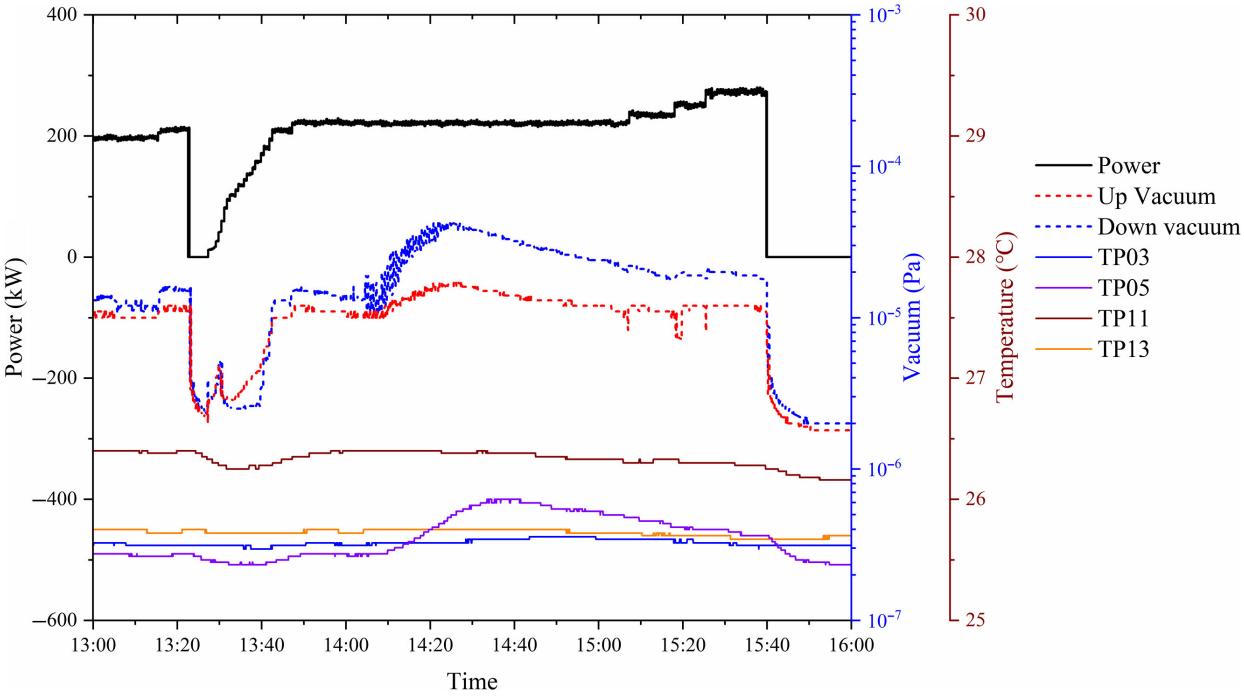

FIG. 25. Typical MP phenomenon encountered during the high power conditioning in traveling wave mode.

conditioned in almost any standing wave state, the phase of the reflection wave was changed by moving the short plate in every 1/32 of the waveguide length (~47.5 mm) from 0 to 1/2 of the waveguide length, and it took about 40 h to complete this work. High power conditioning with 16 different reflection wave phases was finally performed with a duty factor of 3% and a peak power of 500 kW in standing wave mode. We mainly focused on the elimination of the MP phenomenon and the total time consumption was about 30 h in this stage. Thereafter, we increased the rf power from zero to 500 kW and kept the power at 500 kW for more than 50 min; the rf, vacuum, and temperature performance of both FPCs were quite stable, as shown in Fig. 24.

C. MP phenomenon validation

The dc bias voltage ranging from −0.35 to +0.35 kV was applied between the inner and outer conductor of the FPC only in the initial stage with an rf duty factor of 0.25% to avoid frequent vacuum interlocks. Various dc bias voltages were attempted, finally, −0.2 and −0.35 kV voltages were chosen for rf power from 5 to 25 kW and 25 to 300 kW, respectively. As for the rf power higher than 300 kW, no dc bias was applied. According to the high power conditioning process, MP was encountered at a power level of 10–38 kW and 180–290 kW in traveling mode and 20–50 kW and 67–110 kW in standing wave mode. Activities such as vacuum bursts and local overheating were observed. However, no electron activities were observed from the MP monitor. Moreover, signals from temperature probes attached to the surface of the rf window outer conductor showed that there was no overheating phenomenon, we could therefore conclude that there was no MP in the rf window region.

Figure 25 shows a typical MP phenomenon during the test operating in traveling wave mode. We could see that the TP05 value increased with the rf power initially; when the input peak power was kept to 220 kW, the TP05 value rose rapidly to the peak value, accompanied by the vacuum deterioration of the test bench; TP05 value and the vacuum of the coupler then decreased as the power increased, it indicated that the strong MP zones were stepped over. Different from TP05, values of other temperature probes such as TP03, TP11, TP13, and so on changed smoothly

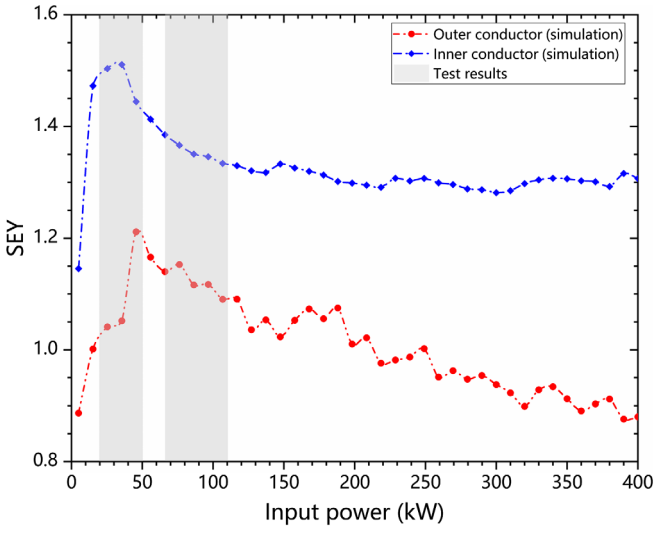

FIG. 26. The simulation and test MP zones.

with the input rf power, and fluctuations of them were relatively stable. We could therefore confirm that the location where MP occurs was in the tapered section of the coaxial line region from Fig. 5. Accordingly, the straight section with a diameter of 60 mm and the tapered section of the coaxial line throughout the high power conditioning process in standing wave mode was the regions where MP occurs. The corresponding MP zones were 20–50 kW and 67–110 kW, respectively, which was consistent with the prediction of the simulation. The comparison between the prediction and the actual encountered MP zones is shown in Fig. 26. All MP barriers were finally eliminated by the high power conditioning process.

VI. CONCLUSION

To satisfy the research of 324-MHz superconducting cavities for CSNS-II and the development of other superconducting cavities working at this frequency, two pulse FPCs with a power capacity of 2 MW are designed, fabricated, and high power conditioned. The coupler has a compact feature that allows it to be preassembled with the cavity in Class 10 clean room, which can effectively reduce cavity contamination. At the same time, the structure between the ceramic window and the coupler mounting port has been optimized to avoid the electron bombardment of the ceramic window due to FE. The system consisting of the test cavity and two couplers has a reflection coefficient of less than -30 dB at the target frequency and an ultimate vacuum better than 3×10^{-7} Pa, which meets the design requirements. FPCs are tested on the test bench at room temperature, and they are high power conditioned up to 2 MW with a duty factor of 1.625% in traveling wave mode and 500 kW with a duty factor of 3% in standing wave mode with 16 different phases of reflection wave. MP barriers encountered during the high power conditioning of FPCs agree reasonably well with the prediction simulated by CST Particle Studio and are finally eliminated by high power conditioning. Considering the successful test of the coupler, we plan to assemble it with the 324-MHz double spoke cavity and the cryostat for the horizontal test at 2 or 4.2 K temperature soon. The hotspot, MP phenomenon, and heat load of the coupler will be focused on during the cryogenic test.

ACKNOWLEDGMENTS

This work is supported by the South Advanced Photon Source Test Facility (SAPS-TF) project and the National Natural Science Foundation of China (Project No. U1832210).

[1] Jie Wei, Hesheng Chen, Yanwei Chen, Yuanbo Chen, Yunlong Chi, Changdong Deng, Haiyi Dong *et al.*, China spallation neutron source: Design, R&D, and outlook, Nucl. Instrum. Methods Phys. Res., Sect. A **600**, 10 (2009).

[2] Quan Zhou, Feisi He, Weimin Pan, Zhongquan Li, and Jisen Yang. Development of a superconducting radio frequency double spoke cavity for CSNS, Nucl. Instrum. Methods Phys. Res., Sect. A **988**, 164873 (2021).

[3] Huachang Liu, Jun Peng, Keyun Gong, Ahong Li, Bo Li, Qiang Chen, Xiaolei Wu *et al.*, The design and construction of CSNS drift tube linac, Nucl. Instrum. Methods Phys. Res., Sect. A **911**, 131 (2018).

[4] K. Akai, N. Akasaka, K. Ebihara, E. Ezura, T. Furuya, K. Hara, K. Hosoyama *et al.*, RF systems for the KEK B-Factory, Nucl. Instrum. Methods Phys. Res., Sect. A **499**, 45 (2003).

[5] Wencan Xu, Z. Altinbas, S. Belomestnykh, I. Ben-Zvi, M. Cole, S. Deonarine, M. Falletta *et al.*, Design, simulations, and conditioning of 500 kW fundamental power couplers for a superconducting rf gun, Phys. Rev. ST Accel. Beams **15**, 072001 (2012).

[6] Isidoro E. Campisi, Fundamental power couplers for superconducting cavities, in *Proceedings of the 10th Workshop on RF Superconductivity (SRF 2001), Tsukuba, Japan* (KEK, Tsukuba, 2001), pp. 132–143.

[7] S. V. Kutsaev, M. P. Kelly, and P. N. Ostroumov, Design of RF power coupler for superconducting cavities, J. Instrum. **7**, P11004 (2012).

[8] Tongming Huang, Pei Zhang, Qiang Ma, Haiying Lin, Qunyao Wang, Weimin Pan, Feng Bing, Kuixiang Gu, and Lin Guo, Development of fundamental power couplers for 166.6 MHz superconducting quarter-wave beta = 1 proof-of-principle cavities, Rev. Sci. Instrum. **91**, 063301 (2020).

[9] Mircea Stirbet, K. M. Wilson, M. Wiseman, J. Henry, M. Drury, G. K. Davis, C. Grenoble *et al.*, RF Conditioning and Testing of Fundamental Power Couplers for SNS Superconducting Cavity Production. In *Proceedings of the 21st Particle Accelerator Conference, Knoxville, TN, 2005* (IEEE, Piscataway, NJ, 2005), pp. 4132–4134.

[10] D. Alesini, *Power coupling* (CERN Accelerator School, Ebeltoft, Denmark, 2010).

[11] Pasi Ylä-Oijala and Marko Ukkola, Suppressing electron multipacting in ceramic windows by DC bias, Nucl. Instrum. Methods Phys. Res., Sect. A **474**, 197 (2001).

[12] Z. Zheng, A. Facco, Z. Liu, J. Popielarski, K. Saito, J. Wei, and Y. Zhang, Prediction and suppression of two-point 1st order multipacting, Nucl. Instrum. Methods Phys. Res., Sect. A **735**, 596 (2014).

[13] M. Fouaidy and N. Hammoudi, RRR of copper coating and low temperature electrical resistivity of material for TTF couplers, Physica (Amsterdam) **441C**, 137 (2006).

[14] Jianrong Zhou, Zhengze Chang, Tongming Huang, Haochen Xu, Keyu Zhu, Mei Li, Liangrui Sun *et al.*, Thermal stability model of power coupler niobium tube for accelerator based on multi-field coupling analysis, Appl. Therm. Eng. **229**, 120633 (2023).

[15] Zhen-Yu Ma and Jin-Fang Chen, Design optimization of 3.9 GHz fundamental power coupler for the SHINE project, Nucl. Sci. Tech. **32**, 132 (2021).

[16] Wencan Xu, J. Fite, D. Holmes, Z. A. Conway, R. A. Rimmer, S. Seberg, K. Smith, and A. Zaltsman, Broadband high power rf window design for the BNL Electron Ion Collider, Phys. Rev. Accel. Beams **25**, 061001 (2022).

[17] CST, https://www.3ds.com.
[18] ANSYS, https://www.ansys.com.
[19] Kui-Xiang Gu, Feng Bing, Wei-Min Pan, Tong-Ming Huang, Qiang Ma, and Fan-Bo Meng, Development of fundamental power coupler for C-ADS superconducting elliptical cavities, Chin. Phys. C **41**, 067001 (2017).
[20] M. Fan, H. Liu, H. Ouyang, A. Li, X. Wu, B. Li, Y. Wang, P. Qu, and Q. Chen, Design of the input power coupler for Boron Neutron Capture Therapy Drift Tube Linac, J. Instrum. **15**, T11007 (2020).
[21] Yuga Nakazawa, Hiromi Iinuma, Yoshihisa Iwashita, Yoshiyuki Iwata, Ersin Cicek, Masashi Otani, Naritoshi Kawamura *et al.*, Multipacting simulations of coaxial coupler for IH-DTL prototype in muon accelerator, J. Phys. Soc. Jpn. Conf. Proc. **33**, 011128 (2021).
[22] Sam Posen and Matthias Liepe, Mechanical optimization of superconducting cavities in continuous wave operation, Phys. Rev. ST Accel. Beams **15**, 022002 (2012).
[23] M. Lynch, S. Kwon, A. Regan, and Y. M. Wang, Excess RF power required for RF control of the spallation neutron source(SNS) linac, a pulsed high-intensity superconducting proton accelerator, *Proceedings of the Particle Accelerator Conference, Chicago, IL, 2001* (IEEE, New York, 2001), Vol. 1, pp. 503–505.
[24] Zhen-Yu Ma, Hong-Tao Hou, Shen-Jie Zhao, Xu-Ming Liu, Yu-Bin Zhao, Sen Sun, Ye-Liang Zhao *et al.*, Manufacturing studies and rf test results of the 1.3 GHz fundamental power coupler prototypes, Phys. Rev. Accel. Beams **25**, 113501 (2022).
[25] Fazhong Shen, Xinbo Wang, Wanzhao Cui, and Lixin Ran, Statistical computation for multipactors in arbitrary microwave devices, IEEE Trans. Microwave Theory Tech. (2023).
[26] S. V. Langellotti, N. M. Jordan, Y. Y. Lau, and R. M. Gilgenbach, CST particle studio simulations of coaxial multipactor and comparison with experiments, IEEE Trans. Plasma Sci. **48**, 1942 (2020).
[27] R. L. Geng, H. Padamsee, S. Belomestnykh, P. Goudket, D. M. Dykes, and Richard G. Carter, Suppression of multipacting in rectangular coupler waveguides, Nucl. Instrum. Methods Phys. Res., Sect. A **508**, 227 (2003).
[28] Tong-ming Huang, Hai-ying Lin, Yi Sun, Jian-ping Dai, Guang-wei Wang, Wei-min Pan, Zhong-quan Li *et al.*, Some experiences with BEPCII SRF System Operation, Chin. Phys. C **40**, 067001 (2016).
[29] Mengxu Fan, Huachang Liu, Ahong Li, Xiaolei Wu, Yun Wang, Peihua Qu, Qiang Chen, and Bo Li, Multipacting study of power couplers for the CSNS DTL, Nucl. Instrum. Methods Phys. Res., Sect. A **953**, 163067 (2020).
[30] V. Baglin, J. Bojko, O. Groebner, B. Henrist, H. Hilleret, C. Scheuerlein, and M. Taborelli, The secondary electron yield of technical materials and its variation with surface treatments, in *Proceedings of the European Particle Accelerator Conference, Vienna, 2000* (EPS, Geneva, 2000), pp. 217–221.
[31] P. N. Ostroumov, S. Kazakov, D. Morris, T. Larter, A. S. Plastun, J. Popielarski, J. Wei, and T. Xu, Suppression of multipacting in high power RF couplers operating with superconducting cavities, Nucl. Instrum. Methods Phys. Res., Sect. A **856**, 77 (2017).
[32] J. Yoon, C. Shik Park, J. Bahng, K.-R. Kim, S. Hee Park, E. Kako, and E.-S. Kim, Development of the antenna adjustable power coupler for 325 MHz superconducting cavities, Nucl. Instrum. Methods Phys. Res., Sect. A **1010**, 165484 (2021).
[33] H. Jenhani, T. Garvey, and A. Variola, RF conditioning studies of input power couplers for superconducting cavities operating in pulsed mode, Nucl. Instrum. Methods Phys. Res., Sect. A **595**, 549 (2008).
[34] S. M. Shajedul Hasan, Y. W. Kang, and M. K. Howlader, Development of an RF conditioning system for charged-particle accelerators, IEEE Trans. Instrum. Meas. **57**, 743 (2008).
[35] Z. Deng, P. Zhang, T. Huang, Q. Wang, H. Lin, J. Dai, Q. Ma, L. Xiao, and W. Pan, Development of an automatic control and analysis system for the conditioning of high-power couplers at IHEP, J. Instrum. **16**, P07027 (2021).